Critical gravitational collapse of a nonminimally coupled scalar field

Erik Jiménez-Vázquez* and Miguel Alcubierre†
Instituto de Ciencias Nucleares, Universidad Nacional Autónoma de México, A.P. 70-543, México D.F. 04510, Mexico

(Received 9 December 2021; accepted 16 March 2022; published 31 March 2022)

We study the critical gravitational collapse of a massless scalar field nonminimally coupled to gravity, using a quadratic coupling function with a strength parameter ξ. We concentrate on critical phenomena of type II, and determine with an accuracy of at least 10^{-12} the value of the critical amplitude for collapse to a black hole, as well as the values of the critical and echoing exponents. Obtaining such high accuracy in the critical amplitude requires us to do a coordinate radial transformation that effectively increases resolution near the central regions by a factor of at least 10^3. As expected, we find that for the case of small coupling the critical behavior is very similar to that of a minimally coupled scalar field. On the other hand, for high coupling the dynamics become so violent that we need to introduce a special slicing condition, known as the shock-avoiding slicing condition, in order to avoid gauge pathologies that would otherwise cause our simulations to fail. With this new gauge condition we are able to perform high-accuracy simulations even in the strong-coupling regime, where we find that the critical and echoing exponents become significantly smaller, and that the echoing behavior is richer and cannot be modeled by a single harmonic.

DOI: 10.1103/PhysRevD.105.064071

I. INTRODUCTION

Studying the gravitational collapse of a real massless scalar field, Choptuik discovered a phenomenon where at the threshold of black hole formation Einstein's field equations have a universal solution, independent of the initial data [1]. Further studies have shown two different types of critical collapse: type I where the black holes have a finite minimum mass, and type II where taking a uniparametric family of initial data parametrized by p, the black hole mass follows a scaling relation of the form

$$M \propto (p - p^*)^{\gamma}, \tag{1}$$

where a black hole forms for $p > p^*$. The critical exponent γ is universal with respect to different families of initial data, depending only on the type of matter. The exact value $p = p^*$ corresponds to a large curvature solution called the "critical solution," which divides the parameter space into two regimes: if $p < p^*$ the original matter content disperses and no black hole is formed, and if $p > p^*$ a black hole is always formed (see for example Ref. [2] for a general review).

The critical solutions also have the property of self-similarity. This symmetry can be either continuous self-similarity (CSS), or discrete self-similarity (DSS). In the discrete case, there exists an echoing exponent Δ such that in logarithmic time,

$$T = -\ln(\tau^* - \tau), \tag{2}$$

the critical solution is periodic in T, with period Δ. In Eq. (2) τ is some measure of time and τ^* is the so-called "accumulation time," i.e., a time where for every small neighborhood there exist infinitely many echoes as we approach from the left $\tau \to (\tau^*)^-$. Usually τ is taken as the proper time of an observer located at the origin. For the case of a real massless scalar field the critical solution has a DSS, and the values of the characteristic exponents have been found to be $\gamma = 0.374$ and $\Delta = 3.445$. These values have been obtained both through direct numerical simulations and using a semianalytical approach [1,3–7]. The DSS found for the case of real massless scalar field is the only possibility when the scalar field is coupled minimally to gravity, but Liebling and Choptuik have shown that in the Brans-Dicke theory, the critical collapse of a scalar field can show both CSS and DSS depending on the value of the coupling parameter [8].

In the spirit of investigating the critical collapse of a real massless scalar field in alternative theories of gravity, we will explore this phenomenon for a generalization of the Brans-Dicke theory, namely the scalar-tensor theories of gravity. Among the many possible modifications to standard general relativity, scalar-tensor theories (STT) are those for which in the so-called Jordan frame representation a scalar field is nonminimally coupled to the Ricci scalar in such a way that it can be understood as a local variation of Newton's constant. Due to these modifications, in STT some phenomena arise that are not present in the standard

*erjive@ciencias.unam.mx
†malcubi@nucleares.unam.mx

general relativity description, such as an extra longitudinal component of gravitational waves [9,10], and also a phenomenon known as "spontaneous scalarization," where self-gravitating solutions with no initial scalar field can spontaneously acquire a nontrivial scalar field that drives the solution into an energetically more favored state. This spontaneous scalarization has been studied for both neutron stars [11,12] and boson stars [13,14]. In a cosmological scenario, STT have been proposed as dark energy models in substitution of the cosmological constant [15–17].

This paper is the organized as follows. In Sec. II we present a brief review of scalar-tensor theories of gravity and the relevant $3+1$ equations. Section III presents our numerical methods, initial data and diagnostics required to find the critical amplitude. We present the results of our numerical simulations in Sec. IV, and we conclude in Sec. V.

II. BASIC EQUATIONS

In this section we summarize the relevant equations that describe the STT of gravity (for more details see for example Refs. [13,18]). The action for scalar-tensor theories with a single scalar field in the Jordan frame is given by (in units such that $c=1$)

$$S=\int\left[\frac{F(\phi)}{16\pi G_0}R-\left(\frac{1}{2}g^{\mu\nu}(\partial_\mu\phi)(\partial_\nu\phi)+V(\phi)\right)\right]\sqrt{-g}dx^4 + S_{\rm mat}(\Psi,g_{\mu\nu}), \tag{3}$$

with ϕ the nonminimally coupled scalar field, $V(\phi)$ a self-interaction potential, R the Ricci scalar of the spacetime, and where $S(\Psi,g_{\mu\nu})$ represents the action of all matter fields other than ϕ. Finally, the function $F(\phi)$ is the nonminimally coupling function, which we have taken to be a quadratic function of the form

$$F(\phi)=1+8\pi\xi G_0\phi^2, \tag{4}$$

with ξ a positive constant. This form of $F(\phi)$ has been used as a toy model for the study of scalarization in both neutron and boson stars [13,14]. In the following we will always consider $V(\phi)=0$, corresponding to a real massless non-interacting scalar field. The constant G_0 is the usual gravitational constant, but notice that in (3) we can identify the "effective" gravitational constant as $G_{\rm eff}=G_0/F(\phi)$.

Varying the action with respect to the spacetime metric and the scalar field one obtains the following field equations:

$$R_{ab}-\frac{1}{2}g_{ab}R=8\pi G_0T_{ab}, \tag{5}$$

$$\Box\phi+\frac{1}{2}f'R=0, \tag{6}$$

with $f:=F/8\pi G_0$, and where f' indicates the derivative of f with respect to the scalar field ϕ, and $\Box=g^{ab}\nabla_a\nabla_b$ is the d'Alambertian operator. The effective stress-energy tensor T_{ab} has three separate contributions given by

$$T_{ab}:=\frac{G_{\rm eff}}{G_0}(T^f_{ab}+T^\phi_{ab}+T^{\rm matt}_{ab}), \tag{7}$$

$$T^f_{ab}:=\nabla_a(f'\nabla_b\phi)-g_{ab}\nabla_c(f'\nabla^c\phi), \tag{8}$$

$$T^\phi_{ab}:=(\nabla_a\phi)(\nabla_b\phi)-\frac{g_{ab}}{2}(\nabla\phi)^2, \tag{9}$$

$$G_{\rm eff}:=\frac{1}{8\pi f}, \tag{10}$$

where $T^{\rm mat}_{ab}$ is the stress-energy tensor of the matter fields other than ϕ. Taking the trace of Eq. (5), one can rewrite the source term in (6) as

$$\Box\phi=\frac{f'T_{\rm matt}-f'(1+3f'')(\nabla\phi)^2}{2f(1+3f'^2/2f)}, \tag{11}$$

with $T_{\rm mat}$ the trace of $T^{ab}_{\rm mat}$. In this context, the Bianchi identities directly imply that the full stress-energy tensor is conserved:

$$\nabla_cT^{ca}=0. \tag{12}$$

Furthermore, the field equations also lead to the conservation of the stress-energy tensor of matter on its own:

$$\nabla_cT^{ca}_{\rm matt}=0, \tag{13}$$

which implies that test particles follow the geodesics associated with the metric g_{ab}.

As usual, we can transform our quantities to the so-called Einstein frame as follows:

$$\tilde{g}_{\mu\nu}:=F(\phi)g_{\mu\nu}, \tag{14}$$

$$\tilde{\phi}:=\int\left[\frac{3}{4}\left(\frac{F'(\phi)}{F(\phi)}\right)^2+\frac{4\pi G_0}{F(\phi)}\right]^{1/2}d\phi, \tag{15}$$

$$W(\tilde{\phi}):=\frac{4\pi G_0\tilde{V}(\tilde{\phi})}{\tilde{F}}, \tag{16}$$

$$\tilde{F}(\tilde{\phi})=F(\phi), \tag{17}$$

so that the action (3) takes the form

$$S[\tilde{g}_{\mu\nu},\tilde{\phi},\psi]=\frac{1}{16\pi G_0}\int[\tilde{R}-2(\tilde{\nabla}\tilde{\phi})^2-4W(\tilde{\phi})]\sqrt{-\tilde{g}}d^4x + S_{\rm matt}[\tilde{g}_{\mu\nu}/\tilde{F}(\tilde{\phi}),\psi], \tag{18}$$

where all quantities with a tilde are computed using the metric $\tilde{g}_{\mu\nu}$ and $\tilde{\phi}$. We prefer not to work in this frame because, as pointed out in [18], even though field equations in the Einstein frame are simpler than those in the Jordan frame, in the Einstein frame the divergence of the matter stress-energy tensor does not vanish [19], i.e., it is not conserved, whereas in the Jordan frame the Bianchi identities guarantee the conservation equations, which in turn imply that Einstein's weak equivalence principle holds.

A. 3 + 1 decomposition

In order to study the evolution in time of our system, we first need to recast the field equations (5) and (6) as a Cauchy problem. We do this by following the $3+1$ formalism [20], and considering a globally hyperbolic spacetime which is foliated by a family of spacelike hypersurfaces Σ_t parametrized by a global time function t. With these considerations, we rewrite the spacetime metric g_{ab} in the form

$$ds^2 = -(\alpha^2 - \beta^i\beta_i)dt^2 + 2\beta_i dx^i dt + \gamma_{ij}dx^i dx^j, \quad (19)$$

with α the lapse function, β^i the shift vector, and γ_{ij} the 3-metric induced on the spatial hypersurfaces. We introduce the unit normal timelike vector n^a to the spacelike hypersurfaces Σ_t, and perform the $3+1$ decomposition via the projection operator $P^a{}_b \coloneqq \delta^a{}_b + n^a n_b$. The extrinsic curvature K_{ab} of the spatial hypersurfaces Σ_t is then given by

$$K_{ab} \coloneqq -P^c{}_a \nabla_c n_b = -(\nabla_a n_b + n_a n^c \nabla_c n_b). \quad (20)$$

For the scalar field it is convenient to introduce the following auxiliary quantities:

$$Q_i \coloneqq D_i\phi = P^k_i \nabla_k \phi, \quad (21)$$

$$\Pi \coloneqq n^a \nabla_a \phi = \frac{1}{\alpha}\frac{d\phi}{dt}, \quad (22)$$

where D_i is the covariant derivative compatible with the 3-metric γ_{ij}, and where we have defied the operator $d/dt \coloneqq \partial_t - \mathcal{L}_\beta$, with $\mathcal{L}_\beta$ the Lie derivative along the shift vector. The evolution equations for Q_i and Π then become

$$\frac{dQ_i}{dt} = D_i(\alpha\Pi), \quad (23)$$

$$\begin{aligned}\frac{d\Pi}{dt} = {}& \alpha[\Pi K + Q^l D_l(\ln\alpha) + D_l Q^l] \\ & - \frac{\alpha}{2f(1+3f'^2/2f)}[2fV' - 4f'V \\ & - f'(1+3f'')(Q^2 - \Pi^2) + f'T_{\rm matt}]. \end{aligned} \quad (24)$$

From the orthogonal decomposition of the stress-energy tensor,

$$T^{ab} = S^{ab} + J^a n^b + n^a J^b + \rho n^a n^b, \quad (25)$$

we obtain the energy density $\rho \coloneqq n^a n^b T_{ab}$, the momentum density $J_a \coloneqq -P^b{}_a n^c T_{bc}$, and the stress tensor $S_{ab} \coloneqq P^c_a P^d_b T_{cd}$. From (7) we see that each component of the stress-energy tensor has three separate contributions:

$$\rho = \frac{G_{\rm eff}}{G_0}(\rho^f + \rho^\phi + \rho^{\rm matt}), \quad (26)$$

$$J_i = \frac{G_{\rm eff}}{G_0}(J^f_i + J^\phi_i + J^{\rm matt}_i), \quad (27)$$

$$S_{ij} = \frac{G_{\rm eff}}{G_0}(S^f_{ij} + S^\phi_{ij} + S^{\rm matt}_{ij}). \quad (28)$$

Using now Eqs. (10) and (11), the explicit expressions for the matter quantities (26)–(28) become

$$\begin{aligned}\rho = {}& \frac{1}{8\pi G_0 f}\left[f'(D_k Q^k + K\Pi) + \frac{\Pi^2}{2} + \frac{Q^2}{2}(1+2f'')\right. \\ & \left. + V(\phi) + \rho_{\rm matt}\right], \end{aligned} \quad (29)$$

$$J_i = \frac{1}{8\pi G_0 f}[-f'(K^k_i Q_k + D_i\Pi) - \Pi Q_i(1+f'') + J^{\rm matt}_i], \quad (30)$$

$$\begin{aligned}S_{ij} = {}& \frac{1}{8\pi G_0 f}\left\{Q_i Q_j(1+f'') + f'(D_i Q_j + \Pi K_{ij})\right. \\ & - \frac{\gamma_{ij}}{(1+3f'^2/2f)}\left[\frac{1}{2}(Q^2 - \Pi^2)\left(1 + \frac{f'^2}{2f} + 2f''\right)\right. \\ & \left.\left. + V(1 - f'^2/2f) + f'V' + \frac{f'^2}{2f}(S_{\rm matt} - \rho_{\rm matt})\right] + S^{\rm matt}_{ij}\right\}, \end{aligned} \quad (31)$$

with $Q^2 \coloneqq Q^l Q_l$, and where $K \coloneqq \gamma^{ij}K_{ij}$ is the trace of the extrinsic curvature tensor.

The $3+1$ evolution equations obtained from the field equation (5) are the standard ADM (Arnowitt-Deser-Misner) equations, given by

$$\frac{d\gamma_{ij}}{dt} = -2\alpha K_{ij}, \quad (32)$$

$$\begin{aligned}\frac{dK_{ij}}{dt} = {}& -D_i D_j\alpha + \alpha[R_{ij} + KK_{ij} - 2K_{il}K^l_j] \\ & + 4\pi G_0\alpha[\gamma_{ij}(S - \rho) - 2S_{ij}], \end{aligned} \quad (33)$$

where R_{ij} is the 3-Ricci tensor associated with the spatial metric γ_{ij}, and $S \coloneqq \gamma^{ij}S_{ij}$. The Hamiltonian and momentum constraints take the form

$$H := \frac{1}{2}(R + K^2 - K_{ij}K^{ij}) - 8\pi G_0 \rho = 0, \tag{34}$$

$$M^i := D_l(K^{il} - \gamma^{il}K) - 8\pi G_0 J^i = 0. \tag{35}$$

Since above we have defined the auxiliary variable Q_i, formally we also need to add its definition (21) and an integrability condition as new constraints:

$$Q_i - D_i\phi = 0, \tag{36}$$

$$D_{[i}Q_{j]} = 0. \tag{37}$$

One final comment about about the well-posedness of the field equations in the Jordan frame. At first sight one might worry that the extra second-order derivative terms that appear in the field equations might affect the well-posedness of the Cauchy problem in this frame. This is one of the reasons why the Einstein frame is usually chosen for analyzing the system. However, the well-posedness of the system in the Jordan frame has already been addressed by Salgado in [21], showing that the field equations in the Jordan frame do indeed form a strong hyperbolic system if one chooses the gauge appropriately (see below).

B. Gauge conditions

Additionally to the evolution equations for the gravitational and scalar fields, in order to obtain a closed evolution system we also have to impose gauge conditions for the lapse α and shift vector β^i. Following [13,21], we will use a modified Bona-Masso slicing condition for the lapse given by

$$\frac{d\alpha}{dt} = -\alpha^2 F_{\rm BM}(\alpha)\left[K - \frac{\Theta}{f_{\rm BM}(\alpha)}\frac{f'}{f}\Pi\right], \tag{38}$$

with $F_{\rm BM}(\alpha)$ a positive but otherwise arbitrary function of α, and Θ an arbitrary parameter. The specific values $F_{\rm BM}(\alpha) = \Theta = 1$ correspond to the so-called "pseudoharmonic" foliation, and have been used in the hyperbolicity analysis in [18,21]. With $\Theta = 0$ one recovers the usual Bona-Masso slicing condition [22], but as shown in [21] in our case this choice does not lead to a strongly hyperbolic formulation. For this reason, in what follows we will always take $\Theta = 1$.

In relation to the choice of the Bona-Masso gauge function $F_{\rm BM}(\alpha)$, one can take

$$F_{\rm BM}(\alpha) = 2/\alpha, \tag{39}$$

which corresponds to the standard $1 + \log$ slicing. However, in Refs. [23,24] one of the authors (M. A.) explored the alternative choice:

$$F_{\rm BM}(\alpha) = 1 + \kappa/\alpha^2, \tag{40}$$

with κ a positive but otherwise arbitrary constant. This choice for $F_{\rm BM}(\alpha)$ is made in order to avoid a particular type of gauge pathologies that lead to singular solutions. These pathologies resemble the shock waves of hydrodynamics, and for this reason are known as "gauge shocks." As we will show below, for some values of the nonminimal coupling constant the evolution using the $1 + \log$ slicing develops a gauge pathology that causes the numerical code to fail. We have found that these gauge pathologies can be eliminated using the gauge function (40). In our simulations below we use this shock-avoiding gauge condition with $\kappa = 1$, so that when $\alpha \to 1$ in the asymptotic region we have $F_{\rm BM} \to 2$, and our gauge condition mimics the standard $1 + \log$ slicing.

Concerning the choice of the shift vector β^i we simply set it to zero since we are mainly interested in subcritical evolutions. For the supercritical case when a black hole forms, a nonzero shift would be preferable in order to avoid the well-known slice stretching effects.

C. Evolution in spherical symmetry

It is well known that the standard ADM formalism results in a weakly hyperbolic formulation of general relativity [20]. Because of this, for our simulations we will use the BSSN (Baumgarte-Shapiro-Shibata-Nakamura) formulation [25,26]. As we are only considering the case of spherical symmetry, we use the generalized version of BSSN formulation which is adapted to curvilinear coordinates [13,27] [28]. Under these assumptions, the conformal 3-metric decomposition takes the form

$$dl^2 = \psi(t,r)^4[A(t,r)dr^2 + B(t,r)r^2 d\Omega^2], \tag{41}$$

where $d\Omega^2 = d\theta^2 + \sin\theta^2 d\varphi^2$ is the solid angle element. The evolution is performed using the spherically symmetric BSSN version of Eqs. (32) and (33), where the energy density, momentum density and stress tensor are given by (29), (30) and (31). Additionally, as we are expecting a spacetime with large gradients of curvature, we will use the puncture method [29] by evolving $\chi = \psi^{-4}$. The Klein-Gordon equation (11) is rewritten as a first-order PD system using (24). Specifically, we evolve the metric quantities A, B, χ, the trace of the extrinsic curvature K, the traceless part of the conformal extrinsic curvature, and the radial component of the conformal connection functions.

III. NUMERICAL SETUP

Numerical simulations are performed using the OllinSphere code presented in [13,30,31]. OllinSphere uses a finite difference method to discretize the Einstein field equations using an equally spaced mesh in r. Following [3,7], we propose a change of coordinates from the original radial coordinate r to a new radial coordinate $\tilde{r}$ which is defined via the differential relation:

$$\frac{dr}{d\tilde{r}} = \frac{1}{1+e^{(\beta\tilde{r}^2+\delta)}}, \tag{42}$$

where β and δ are arbitrary constants such that $\beta < 0$ and $\delta > 0$. With this transformation, as $\tilde{r}$ approaches infinity we have $dr/d\tilde{r} \to 1$. On the other hand, as $\tilde{r} \to 0$, the relation (42) approaches

$$\frac{dr}{d\tilde{r}} = \frac{1}{1+e^{\delta}} - \frac{\beta e^{\delta}\tilde{r}^2}{(1+e^{\delta})^2} + \mathcal{O}(\tilde{r}^4), \tag{43}$$

showing that the parameter δ adjusts the resolution near the origin $\tilde{r} = 0$, while β measures how fast $dr/d\tilde{r}$ approaches 1 far away. The typical values we use for our simulations are $\delta = 5, \beta = -1$. With these choices, a uniform grid on $\tilde{r}$ becomes nonuniform in r, gaining a factor of about 10^3 times more resolution close to the origin. One final comment related to Eq. (42): As this expression is not analytically integrable, the differential relation must be solved numerically. In order to reduce numerical error up to machine precision we integrate this equation with a Chebyshev quadrature starting from the origin, using a fifth-order Chebyshev polynomial between each grid point.

Using the change of coordinates given by (42) does not require any change in the internal structure of the OllinSphere code, as it already uses the most general form of the line element in spherical symmetry for the conformal metric:

$$ds_3^2 = A(t,r)dr^2 + B(t,r)r^2 d\Omega^2, \tag{44}$$

with A and B positive metric functions, and $d\Omega^2 = d\theta^2 + \sin\theta^2 d\varphi^2$ the solid angle element. Once we have some initial data (see next section), changing the radial coordinate from r to $\tilde{r}$ modifies the explicit values of the metric coefficients A and B, but the new metric has exactly the same form as above with new metric coefficients given by

$$\tilde{A} \coloneqq A\left(\frac{dr}{d\tilde{r}}\right)^2, \qquad \tilde{B} \coloneqq B\left(\frac{r}{\tilde{r}}\right)^2. \tag{45}$$

A. Initial data

As mentioned before, the matter content in our numerical simulation consists of a massless scalar field coupled nonminimally to gravity. For the scalar field we consider the following initial data profiles:

$$\phi_I(0,r) = \phi_0 e^{(-r^2/\sigma^2)}, \tag{46}$$

$$\phi_{II}(0,r) = \phi_0 r^2 e^{(-r^2/\sigma^2)}, \tag{47}$$

$$\phi_{III}(0,r) = \phi_0 \coth(s_0/\sigma)\left[\tanh\left(\frac{r+s_0}{\sigma}\right) - \tanh\left(\frac{r-s_0}{\sigma}\right)\right], \tag{48}$$

where r, σ, s_0 are free parameters. In our numerical simulations we fix $\sigma = 1$, $s_0 = 0.5$, and use the amplitude ϕ_0 as the tuning parameter for the initial pulse.

The conformal metric is initialized to the flat metric in spherical symmetry, that is $A = B = 1$. However, once we change to the rescaled radial coordinate $\tilde{r}$ this implies that

$$\tilde{A} = (dr/d\tilde{r})^2, \qquad \tilde{B} = (r/\tilde{r})^2. \tag{49}$$

We also assume time-symmetric initial data, which imply that the momentum constraint (35) is trivially satisfied. This leaves the Hamiltonian constraint (34) as the only equation to solve for the initial conformal factor $\psi(\tilde{r})$. Boundary conditions for ψ are obtained from the asymptotic flatness condition:

$$\psi(\tilde{r})|_{\tilde{r}\to\infty} = 1. \tag{50}$$

In practice, however, we use a boundary condition at a finite radius of the form

$$\partial_{\tilde{r}}\psi = \frac{1-\psi}{\tilde{r}}, \tag{51}$$

which is a Robin-type boundary condition and reflects the fact that as $\tilde{r} \to \infty$ we have $\psi \to 1 + \mathcal{O}(r^{-1})$. At the origin, we demand that ψ must be an even function in $\tilde{r}$ for regularity, that is,

$$\partial_{\tilde{r}}\psi(\tilde{r})|_{\tilde{r}=0} = 0. \tag{52}$$

Additionally, the initial gauge is completely specified by choosing a precollapsed lapse of the form $\alpha = \psi^{-2}$, as well as zero shift vector $\beta^i = 0$.

B. Diagnostics

The final state of the evolution is determined by the strength of the initial data. For a critical value of the amplitude ϕ_0^* one finds that weak initial data with $\phi_0 < \phi_0^*$ completely disperse leaving behind Minkowski spacetime, while for stronger initial data with $\phi_0 > \phi_0^*$ the scalar field collapses to form black hole. The critical value ϕ_0^* is found using a bisection method, bracketing the interval between an amplitude for which the scalar field is dispersed ϕ_d, and an amplitude ϕ_c for which a black hole forms. In a similar way to [7], the dimensionless quantity

$$\delta\phi = \frac{\phi_c - \phi_d}{\phi_d} \tag{53}$$

indicates the precision with which we have found the critical amplitude. In order to obtain the critical exponents we need an accuracy equal to or better than $\delta\phi \sim 10^{-6}$. Increasing precision leads to longer evolutions near the

critical solution, resulting in less uncertainty in the estimation of the critical exponent γ and echoing parameter Δ.

The final state of the evolution is analyzed looking at the behavior of the lapse at the origin. If the initial data are dispersed, the lapse will return to 1 as the spacetime approaches Minkowski. On the other hand, if a black hole forms our gauge condition causes the lapse to collapse to zero at the center. In order to better study the collapsing configurations, we also search for an apparent horizon at every time step. This is done by calculating the expansion of outgoing null geodesics and looking for a place where it becomes zero. In spherical symmetry this expansion takes the form

$$\Theta = \frac{1}{\psi^2\sqrt{A}}\left(\frac{2}{r} + \frac{\partial_r B}{B} + 4\frac{\partial \psi}{\psi}\right) - 2K^\theta_\theta = 0, \quad (54)$$

where K^θ_θ is the angular component of the extrinsic curvature with mixed indices. Since our study only focuses on subcritical evolutions, we do not need to determine very accurately the final mass of the formed black hole.

In the subcritical regime, since $\xi = 0$ corresponds to the minimally coupled case, we expect that the maximum value of the 4D-Ricci scalar evaluated at the origin will follow a scaling law corresponding to a type II critical collapse:

$$R_{\max} \simeq |\phi_0^* - \phi_0|^{-2\gamma}, \quad (55)$$

where the factor -2 in the scaling exponent is there because the 4D-Ricci scalar has units of length to the minus two. Additionally to this behavior, Hod and Piran [32] noticed that for a scalar field coupled minimally to gravity, the self-discrete nature of the critical phenomena adds a periodic modulation to the scaling law. The 4D-Ricci scalar is then expected to behave as

$$\ln R_{\max} = c - 2\gamma \ln|\phi_0^* - \phi_0| + f(\ln|\phi_0^* - \phi_0|), \quad (56)$$

with c a constant that depends on the initial data family, and where $f(x)$ is a periodic function with a frequency given by

$$\omega = \frac{\Delta}{2\gamma}, \quad (57)$$

with Δ the so-called echoing exponent. Usually, to first order one can approximate $f(x)$ by a simple trigonometric function, for example:

$$f(x) = a_0 \sin(\omega x + \varphi). \quad (58)$$

The 4D-Ricci then behaves as

$$\ln R_{\max} = c - 2\gamma \ln|\phi_0^* - \phi_0| + a_0 \sin(\omega \ln|\phi_0^* - \phi_0| + \varphi_0), \quad (59)$$

where the constants c, a_0, φ_0 are family dependent. Fitting the function (59) provides us with a first method to compute the echoing exponent Δ. But there is a second method one can use to find Δ due to Baumgarte [33]. One can consider the times for two pairs of consecutive zero crossings of the scalar field ϕ evaluated at the origin, (τ_n, τ_{n+1}) and (τ_m, τ_{m+1}). Substituting these values in the logarithmic time (2) we will then have the corresponding pairs (T_n, T_{n+1}), (T_m, T_{m+1}). Assuming now that each pair differs in half the period $\Delta/2$, one can solve for the accumulation time τ^*, obtaining

$$\tau^* = \frac{\tau_n\tau_{m+1} - \tau_{n+1}\tau_m}{\tau_n - \tau_{n+1} - \tau_m + \tau_{m+1}}. \quad (60)$$

This estimation for the accumulation time also provides us with an estimate of the echoing period Δ given by

$$\Delta = 2\ln\left(\frac{\tau^* - \tau_n}{\tau^* - \tau_{n+1}}\right). \quad (61)$$

IV. NUMERICAL RESULTS

All our simulations have been performed using a method of lines with a fourth-order Runge-Kutta integration in time, and fourth-order centered finite differences in space. Values for the nonminimal coupling constant ξ in (4) were chosen in a logarithmic scale, taking as specific values $\xi = 10^{-3}, 10^{-2}, 10^{-1}, 1, 10$. For our simulations we use a grid spacing of $\Delta r = 0.005$, with $N_r = 2800$ points in the radial direction, and the parameters used by the radial coordinate transformation are $\delta = 5$ and $\beta = -1$. Additionally, we have used an adaptive time step in order to always satisfy the Courant-Friedrich-Levy condition required for numerical stability [20].

Critical phenomena can be strongly affected by numerical error due to either the boundary conditions or the finite difference method. The first source of error can be highly reduced by using constraint-preserving boundary conditions. These have been implemented using the algorithm described in [13,30], reducing by a factor of about 10^3 the error introduced by the artificial boundary in comparison with the standard Sommerfeld (radiative) boundary conditions. In relation to the error introduced by the finite difference method, we also use sixth-order Kreiss-Oliger dissipation in order to be compatible with the fourth-order discretization. This artificial dissipation dampens high-frequency modes which would otherwise spoil the evolution near the black hole formation threshold.

For each value of the coupling constant ξ we test the three different families of initial data given by Eqs. (46), (47), and (48). Reported values for the critical exponents (γ, Δ) are the averages of the critical exponents obtained for each family, and the uncertainty is taken as the highest deviation from this mean value, although we will only show

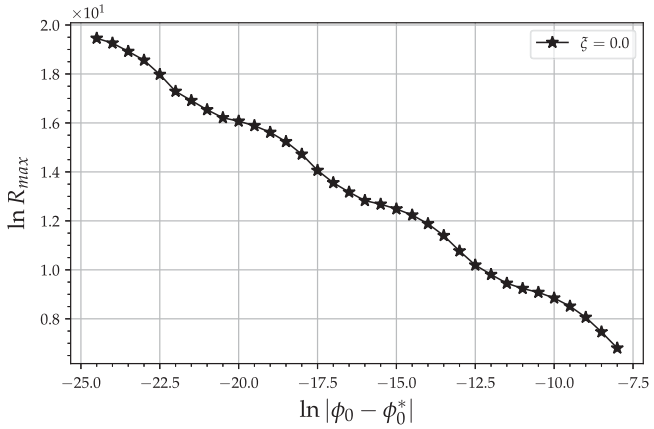

FIG. 1. Scaling of the maximum value at the origin of the 4D-Ricci scalar for a minimally coupled scalar field ($\xi = 0$) field. The plot corresponds to the subcritical case, and the dots are equally spaced along the $\ln|\phi_0 - \phi_0^*|$ axis.

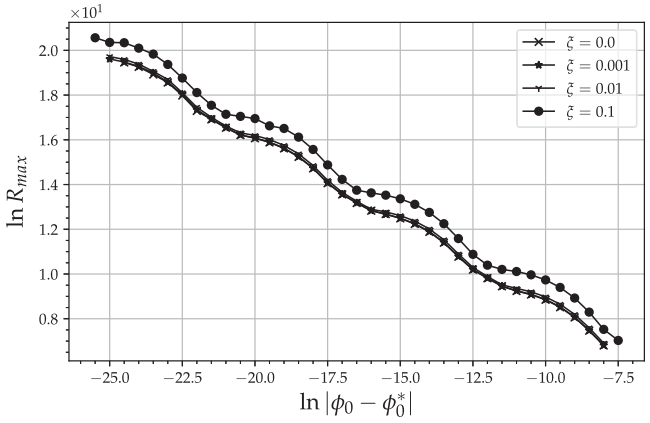

FIG. 3. Same as Fig. 1, but for different values of the coupling parameter $\xi = 0, 10^{-3}, 10^{-2}, 10^{-1}$. All curves shows the same slope and oscillation period.

plots for family I. In each case we find the critical amplitude with a precision about $\delta\phi \approx 10^{-12}$.

In order to have a basis for comparison, we first analyze the case of a massless scalar field coupled minimally to gravity corresponding to $\xi = 0$, using the $1 + \log$ slicing condition. Figure 1 shows the maximum value of the 4D-Ricci scalar at the origin for a subcritical evolution in this case. Fitting the function (59) allows us to find the critical exponents $\gamma \approx 0.374 \pm 0.001$ and $\Delta \approx 3.45 \pm 0.005$, which are in excellent agreement with those reported in [7,34], and for which a semianalytical calculation gives $\gamma = 0.374 \pm 0.001$ and $\Delta = 3.4453 \pm 0.0005$. Figure 2 shows the central value of the scalar field for a simulation with an initial amplitude $\phi_0 = 0.303350064438822$, which we are taking as the critical solution, versus the logarithmic time T defined in (2). For this case we can also use the second method for calculating the echoing exponent using Eqs. (60) and (61), obtaining $\Delta = 3.42 \pm 0.003$, again in good agreement with previous results.

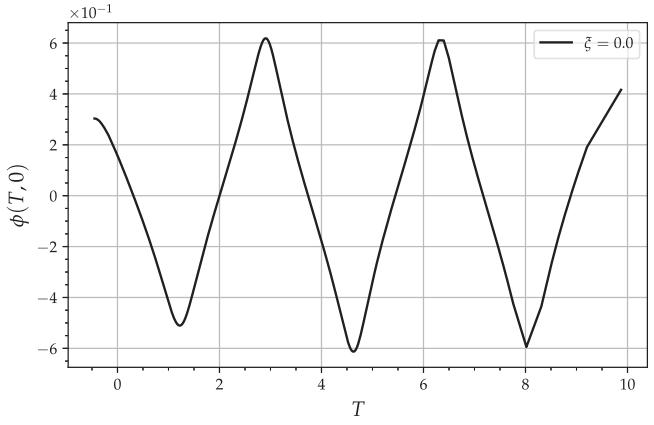

FIG. 2. Central value of the minimally coupled scalar field vs logarithmic time T, clearly showing the periodic behavior of the scalar field.

Next we consider the values $\xi = 10^{-3}, 10^{-2}, 10^{-1}$ for the nonminimal coupling parameter in Eq. (4), again using the $1 + \log$ slicing condition. Results of the maximum value of the 4D-Ricci scalar at the origin for each value of ξ are shown in Fig. 3, where we also include the case $\xi = 0$ for comparison. In the same way as before, we fit the function (59) and obtain the critical exponents (γ, Δ), and we also use Eqs. (60) and (61) for a second estimate of Δ. Our results are summarized in Table I. Figure 4 also shows the echoing behavior of the value of the scalar at the origin as a function of logarithmic T. For all these evolutions we obtain a critical exponent $\gamma \approx 0.374$, with an uncertainty of less than 0.3%. Also, the echoing exponent is almost exactly equal in all three cases up to a small uncertainty. We then find that there are no major differences in the critical behavior when compared to the minimally coupled case.

Values of the coupling parameter such that $\xi \geq 1$ require a different treatment than the previous cases. For the particular case with $\xi = 1$ using a $1 + \log$ slicing condition we find that, while bracketing the critical amplitude using the bisection method, once we reach a precision in the amplitude close to $\delta\phi \approx 10^{-3}$ the numerical code crashes and our simulations fail. For example, when using the initial data family I [Eq. (46)] with an initial amplitude of $\phi_0 = 0.2354$, we find that the lapse α, the conformal metric

TABLE I. Critical exponent γ and echoing exponent Δ (obtained by two different methods), for different values of the coupling parameter in (4). The three cases $\xi = 10^{-3}, 10^{-2}, 10^{-1}$ have the same critical exponents up to a small uncertainty.

ξ	γ	Δ (59)	Δ (61)
0.001	0.374 ± 0.001	3.441 ± 0.001	3.446 ± 0.004
0.01	0.374 ± 0.001	3.442 ± 0.007	3.446 ± 0.002
0.1	0.372 ± 0.004	3.442 ± 0.003	3.445 ± 0.005

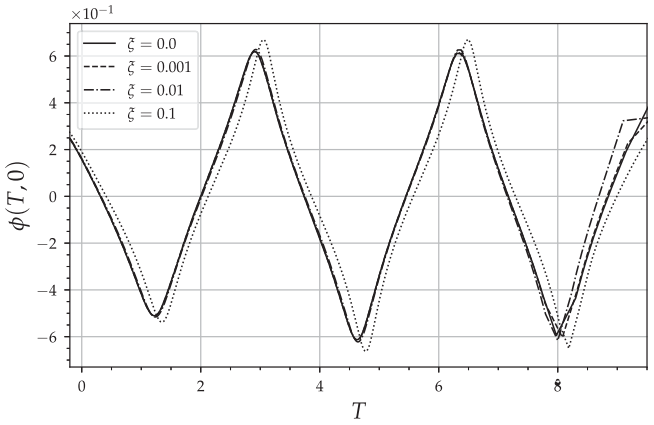

FIG. 4. Central value of the scalar field plotted vs logarithmic time T for $\xi = 0, 10^{-3}, 10^{-2}, 10^{-1}$, showing the periodic behavior of the scalar field.

coefficient $\tilde{A}$, and the trace of extrinsic curvature tr$K$ all develop very large gradients at $\tilde{r} \approx 2.55$ that cause the code to crash at a coordinate time $t \approx 3.53$. We have found that these large gradients in fact becomes worse as we increase our numerical resolution. This is shown in Fig. 5, where we plot results from three different resolutions: $\Delta\tilde{r} = 0.02, 0.01, 0.005$. This behavior is quite similar to the "gauge shocks" described by one of the authors in [23,24], as well as the problems reported by Hilditch *et al.* in [35] while evolving near-critical Brill wave spacetimes [36,37].

We have in fact traced the problem with these large gradients to the choice of the $1 + \log$ slicing condition, and have therefore changed our gauge choice to the "shock-avoiding" lapse $f_{\rm BM}(\alpha) = 1 + 1/\alpha^2$ described in Eq. (40) (with $\kappa = 1$). In order to compare both slicing conditions we also evolved the case $\xi = 0$ using the shock-avoiding slicing condition, obtaining the critical exponents $\gamma = 0.374 \pm 0.003$ and $\Delta = 3.44 \pm 0.005$. Figure 6 shows the critical behavior using both lapse conditions for the initial data family I. The top panel shows a comparison of the scaling of the maximum central value of the 4D-Ricci scalar for both slicings, while the lower panel shows the absolute difference between them. Although in the lower panel of the figure some sharp peaks can be observed, the maximum absolute difference is only about 6×10^{-2}, implying a maximum percentage difference of less than 0.3%. These peaks occur mostly for simulations that are extremely close to the critical solution, and are probably due to the high sensitivity of the results on the numerical method, particularly when obtaining the maximum value of the Ricci scalar which can become quite large. Still, one can clearly see from the top panel of the figure that both slicing conditions give very similar results.

Changing to the shock-avoiding slicing condition now also allows us to evolve the case with $\xi = 1$ and $\phi_0 = 0.2354$ that we mentioned above until a black hole is formed at $t \approx 5.5$, thus showing that this in fact corresponds to a supercritical case. As was already pointed out in [24], one possible problem with the shock-avoiding slicing condition is that lapse is now allowed to take negative values. We can see that this is indeed the case in Fig. 7, where we plot the central value of the lapse as a function of

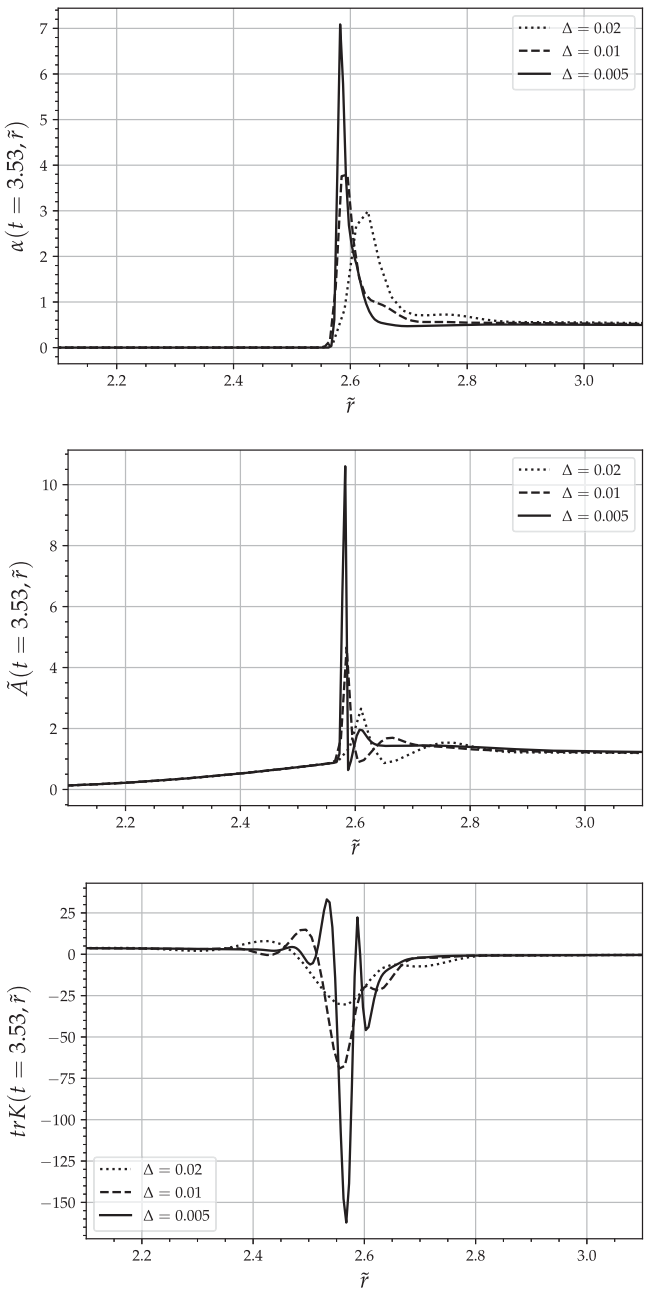

FIG. 5. Snapshots of the lapse function α, the conformal radial metric coefficient $\tilde{A}$, and the trace of the extrinsic curvature tr$K$, at coordinate time $t \approx 3.53$, for $\xi = 1$ and initial data of type I with $\phi_0 = 0.2354$, using a $1 + \log$ slicing condition and three different resolutions. We can see that all three functions develop large gradients close to $\tilde{r} \approx 2.55$, that in fact become worse with increased resolution. These gradients cause the simulations to fail shortly after this time.

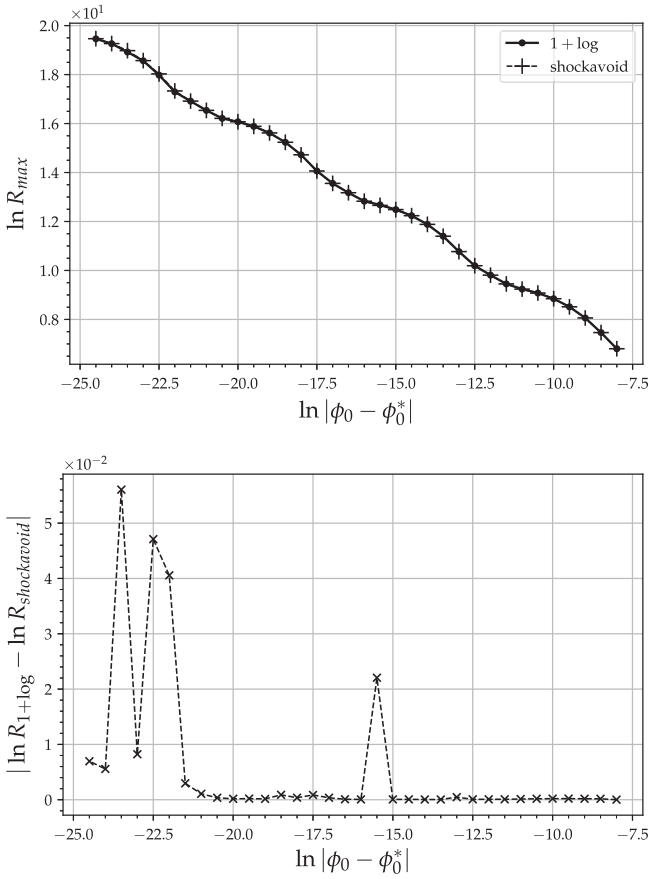

FIG. 6. Top panel: 4D-Ricci scaling for the subcritical case with coupling parameter $\xi = 0$, using both the $1 + \log$ and shock avoiding slicing conditions. Bottom panel: Absolute value of the difference between both plots on a logarithmic scale.

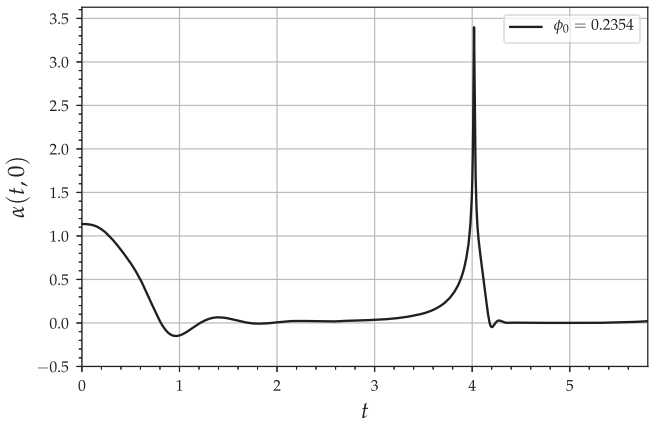

FIG. 7. Lapse function α evaluated at the origin using the shock-avoiding slicing condition for the case with $\xi = 1$ and $\phi_0 = 0.2354$. Using this condition the lapse becomes negative at coordinate time $t \approx 0.8$, but it quickly returns to positive values. The negative values of the lapse do not seem to cause any problems with the simulation.

coordinate time for this same simulation. We have found that having the lapse sometimes become negative in the central regions does not in fact seem to cause any problems. Quite the opposite, the negative values of the lapse helps to avoid the large gradients that caused the simulations to crash with the $1 + \log$ slicing condition. The negative lapse would seem to make the slices back away from a possible coordinate singularity, and later start moving forward again.

Using the shock-avoiding slicing condition we have been able to perform simulations with much larger values of the coupling parameter ξ, and have accurately determined the critical exponents. The critical behavior for the cases with $\xi = 1,\ 10$ is shown in Fig. 8, which plots the scaling of the maximum value of the 4D-Ricci scalar for these cases. Even by eye one can see that the plot now shows at least two different superposed oscillation frequencies. This can be seen more clearly after subtracting a linear fit from the numerical data, as shown in Fig. 9. This observation is further confirmed by applying a fast Fourier transform

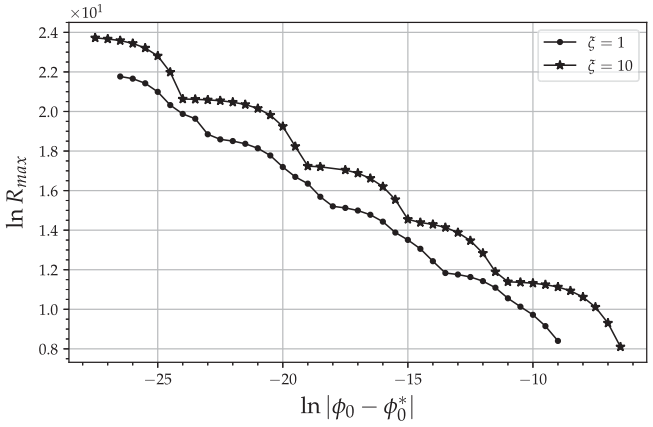

FIG. 8. 4D-Ricci scaling for the subcritical case with coupling parameters $\xi = 1,\ 10$.

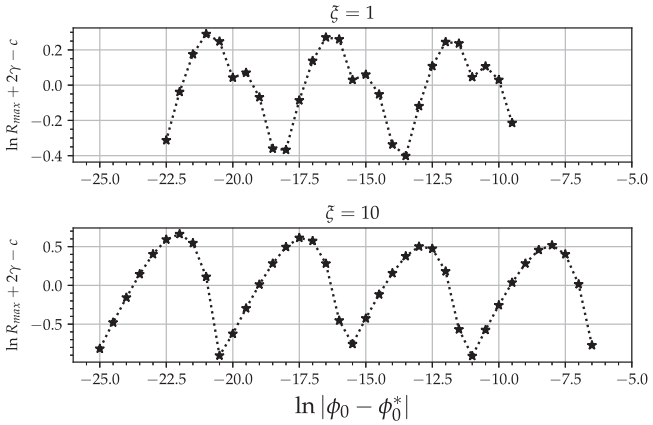

FIG. 9. Same data as in Fig. 8 after subtracting a linear fit. The top panel shows the case for $\xi = 1$, while the bottom panel shows the case for $\xi = 10$.

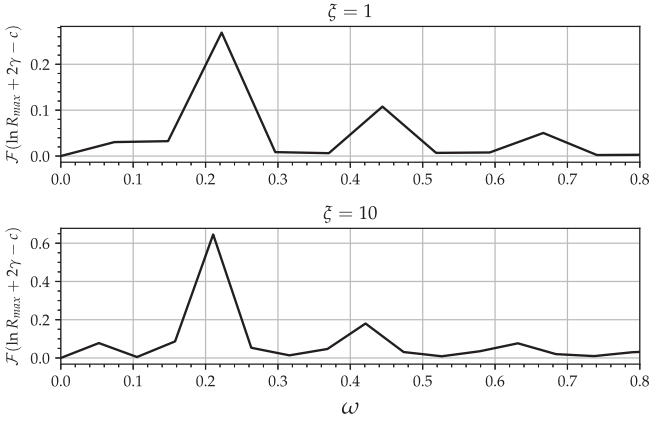

FIG. 10. Fourier transforms of the data shown in Fig. 8. One can clearly see a fundamental frequency plus at least its first two harmonics.

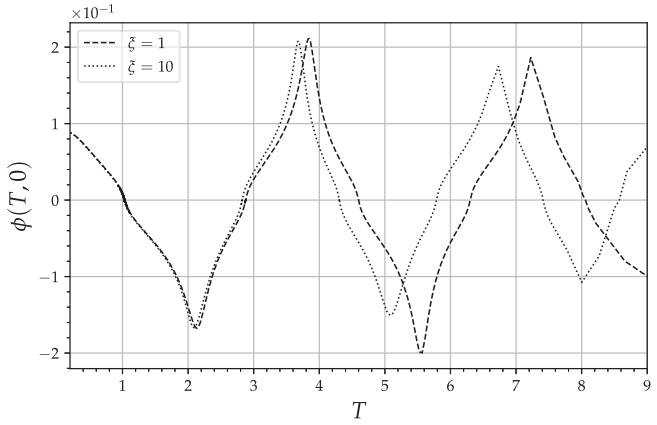

FIG. 11. Central value of the scalar field plotted vs logarithmic time T for $\xi = 1$, 10, showing the periodic behavior of the scalar field.

(FFT) to the data after subtracting a linear fit of the form $2\gamma \ln|\phi_0 - \phi_0^*| + c$. Results of this FFT can be seen in Fig. 10, which clearly reveals the presence of a fundamental frequency ω and at least the first two harmonics.

In fact, the difference of the 4D-Ricci scaling from the linear fit for the case with $\xi = 10$ resembles a smooth sawtooth. From Fig. 10 we can observe that the highest peaks in the Fourier transform are at frequencies ω and 2ω. Accordingly, instead of just fitting a function of the form (59), we add a second term with frequency 2ω:

$$\ln R_{\max} = C - 2\gamma \ln|\phi_0^* - \phi_0| + a_0 \sin(\omega \ln|\phi_0^* - \phi_0| + \varphi_0) + a_1 \sin(2\omega \ln|\phi_0^* - \phi_0| + \varphi_1). \quad (62)$$

Table II shows our results for the cases $\xi = 1$, 10. The uncertainty in the critical exponent γ in each case is less than %2, although the echoing exponent Δ could not be so accurately determined having an uncertainty of about %6. Figure 11 also shows the periodic behavior of ϕ in logarithmic time T for these two cases.

Considering only the cases shown in Tables I and II, one can observe a decrease in the critical exponent values, even though the strong-coupling cases $\xi = 1$, 10 require a better study. Also, for the cases with a stronger coupling it is clear that the second harmonic of the fundamental frequency cannot be neglected in the 4D-Ricci scaling.

TABLE II. Critical exponent γ and echoing exponent Δ (obtained by two different methods), for values of the coupling (4) $\xi = 1$, 10.

ξ	γ	Δ (62)	Δ (61)
1	0.368 ± 0.001	3.386 ± 0.017	3.450 ± 0.080
10	0.365 ± 0.006	3.109 ± 0.007	2.981 ± 0.193

V. CONCLUSION

We performed numerical simulations for the critical collapse of a nonminimally coupled massless scalar field with a quadratic coupling function, using a BSSN code adapted to spherical symmetry. Although the original structure of the code uses a uniform radial grid, the extremely high resolution needed for evolving the data in the threshold of black hole formation required us to employ a coordinate transformation in the radial direction. With this modification we gain a factor of about 10^3 times more resolution near the origin when compared to the original grid. In all cases the value of the critical amplitude is found to an accuracy of approximately $\delta\phi \approx 10^{-12}$.

We find that for small values of the coupling parameter $\xi < 1$, the results obtained for both the critical exponent γ and echoing exponent Δ show no significant difference from the case of a massless minimally coupled scalar field. On the other hand, for values of the coupling parameter such that $\xi \geq 1$ we have found that, when using the $1 + \log$ slicing condition, large gradients develop in the lapse, the conformal coefficient metric $\tilde{A}$, and the trace of extrinsic curvature $\mathrm{tr}K$, that cause the numerical code to crash and severely limit the accuracy with which we can find the critical amplitude to only about $\delta\phi \approx 10^{-3}$. Further analysis shows that these large gradients are even sharper at higher numerical resolutions, resembling results obtained in the study by Hilditch *et al.* on Brill waves [35]. For this reason, in the case of large coupling parameters we have switched to using the so-called shock-avoiding slicing condition introduced in [23,24] in order to avoid a particular class of gauge pathologies known as gauge shocks.

Using this new slicing condition we have been able to follow much further the simulations with strong-coupling parameters and have been able to determine the critical amplitude with high accuracy. This has allowed us also to find both the critical exponent and echoing exponent,

showing a decrease in their values as the coupling parameter ξ increases. Furthermore, we have also found that for strong couplings the periodic function which appears in the scaling of the 4D-Ricci scalar could not be simply approximated by a single sine function. After performing a Fourier transform we observe that this scaling also has important contributions from the second harmonic of the fundamental frequency, and maybe even from the third.

In summary, our results show that for small coupling parameters the simulations are very similar to the case of a minimally coupled scalar field, while for the case of large coupling parameter the evolution is significantly more complex, leading to stronger dynamics that require the use of improved gauge conditions, and resulting in a modification of the critical exponents as well as a richer periodic structure in the echoes of the scalar field.

One final comment about the fact that while using the shock-avoid slicing condition (40) the lapse function can sometimes become negative. Allowing for negative values of the lapse implies that the spatial slices will sometimes evolve backwards in time for a while before moving forward again. Such behavior can introduce some spurious oscillations that might complicate the analysis of the critical collapse. This is shown in Fig. 12, where one can see that at each zero crossing of the nonminimally coupled (NMC) scalar field at the origin, there are small oscillations around zero, possibly due to the negative values of the lapse. Because of this, in Eq. (60) instead of using consecutive zero crossings of the scalar field, we have used the maximum values of the absolute value of the NMC scalar field. In order to make sure that the negative values of the lapse do not affect our results we just need to verify that for each two arbitrary pairs (N, M) of the maximum absolute value of the scalar field, which occur at coordinate times (t_N, t_m) and corresponding proper times at the origin (τ_N, τ_M), if we have $t_N < t_M$ then we also have $\tau_N < \tau_M$.

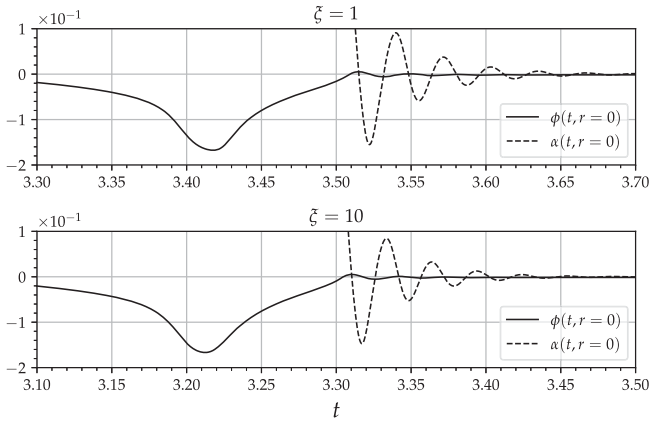

FIG. 12. Central value of the scalar field plotted for coupling values $\xi = 1$, 10 with their respective value of the lapse. The scalar field develops small oscillations around zero due to the negative value of the lapse.

ACKNOWLEDGMENTS

This work was partially supported by CONACyT Network Projects No. 376127 and No. 304001. E. J.-V. was also supported by a CONACyT National Graduate Grant.

APPENDIX: EINSTEIN FRAME ANALYSIS

Using Eqs. (14) and (15) we can also repeat our analysis of the critical behavior in the Einstein frame, but now using the quantities $\tilde{\phi}$ and $\tilde{R}$. In the Einstein frame, the scalar field (15) with coupling function (4) can be approximated for $\xi \ll 1$ as

$$\tilde{\phi} = 2\sqrt{\pi}\phi - \frac{8}{3}(G_0\pi^{3/2}\phi^3)\xi + \mathcal{O}(\xi^{3/2}). \tag{A1}$$

Since the maximum value of $|\phi|$ is of order 10^{-1}, $\tilde{\phi}$ and ϕ are related up to a scaling factor plus some negligible terms. Also, from (14), the proper time in the Einstein frame τ_E for $\xi \ll 1$ will be approximately equal to the proper time in the Jordan frame τ_J, up to second order in ξ. This implies that the zero crossings for $\tilde{\phi}$ will occur at the essentially same proper time in both frames, so we expect that the echoing exponents in both frames will be the same up to second order in ξ^2 for $\xi \ll 1$. As was done before, we estimate the echoing period by analyzing the periodic behavior in the Ricci scalar $\tilde{R}$, which can be computed through

$$\tilde{R} = \frac{1}{8\pi G_0 f}\left[R\left(1 + \frac{3}{2}\frac{f'^2}{f}\right) - \frac{3}{2}\left(\frac{2ff'' - f'^2}{f^2}\right)g^{\mu\nu}\partial_\mu\phi\partial_\nu\phi\right]. \tag{A2}$$

Figure 13 shows the scaling behavior of $\tilde{R}_{\max}$. Even by eye we can see that the critical exponents are very similar to each other. Next, we subtract a linear fit to highlight the periodic behavior. The resulting functions are shown in Fig. 14.

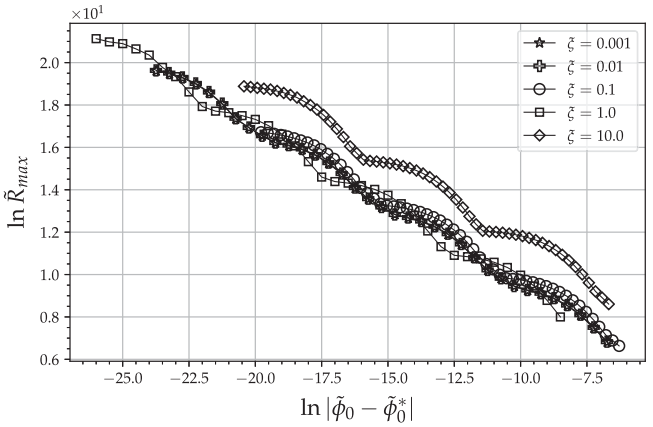

FIG. 13. Scaling of the maximum value of the Ricci scalar in the Einstein frame for different coupling values.

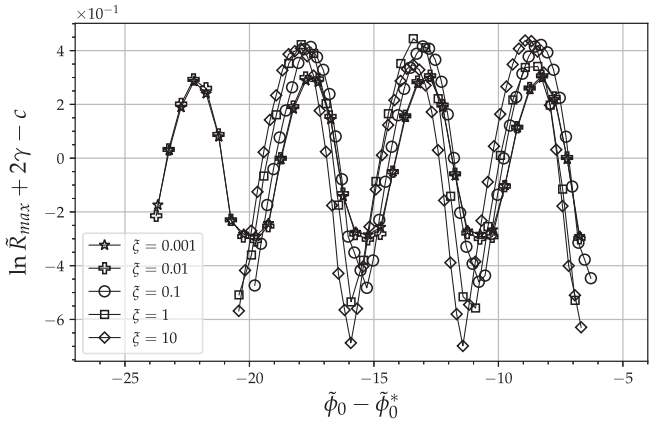

FIG. 14. The scaling curves shown in Fig. 13 minus a linear fit, for all coupling values.

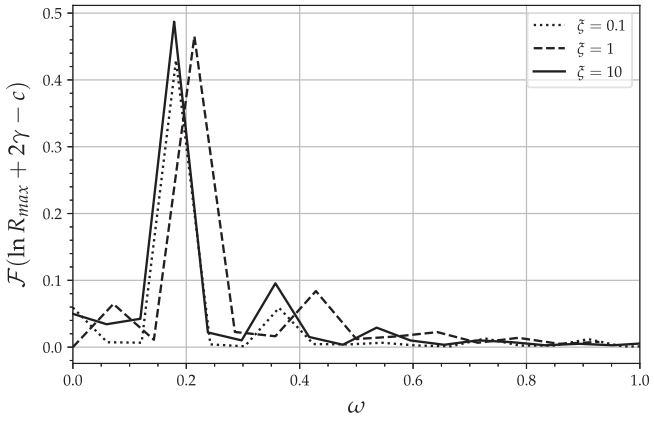

FIG. 15. Fourier transformation of the data shown in Fig. 14 for $\xi = 0.1$, 1, 10. We can see the fundamental frequency plus a harmonic with the double frequency of the fundamental.

TABLE III. Same as Tables I and II, but now in the Einstein frame.

ξ	γ	Δ (59)	Δ (61)
0.001	0.374 ± 0.002	3.443 ± 0.002	3.444 ± 0.006
0.01	0.374 ± 0.003	3.441 ± 0.005	3.445 ± 0.003
0.1	0.374 ± 0.003	3.448 ± 0.003	3.445 ± 0.002
1	0.371 ± 0.003	3.425 ± 0.005	3.420 ± 0.008
10	0.369 ± 0.002	3.412 ± 0.017	3.271 ± 0.132

After applying a Fourier transform to the curves shown in Fig. 14, we find that for the cases $\xi = 0.001, 0.01$ obtains only one frequency mode that characterizes the periodic behavior, so that we can fit the Ricci scalar with a function of the form (59). For $\xi \geq 0.1$, we obtain a second frequency which is the double of the fundamental frequency as we show in Fig. 15, so that in these cases we fit the behavior using a function of the form (62). In particular, we see that for these cases, while in both the Jordan and Einstein frames there exists a second-harmonic frequency, the amplitude of the second harmonic is considerably smaller in the Einstein frame. Interestingly, we also find that for the case $\xi = 0.1$ there is a clear contribution from a second harmonic in the Einstein frame which was not apparent in the Jordan frame. At this point we are unsure as to how to interpret these differences. It could have something to do with the fact that in the Jordan frame the effective gravitational constant oscillates with the scalar field, while in the Einstein frame it does not.

Finally, our results for γ and Δ are presented in Table III. As done in the Jordan frame, we use (61) to obtain a second estimation for the echoing period Δ. As expected, for $\xi = 0.001, 0.01\gamma$ and Δ are very similar to that obtained in the Jordan frame.

[1] M. W. Choptuik, Phys. Rev. Lett. **70**, 9 (1993).
[2] C. Gundlach and J. M. Martin-Garcia, Living Rev. Relativity **10**, 5 (2007).
[3] O. Rinne, Gen. Relativ. Gravit. **52**, 117 (2020).
[4] C. Gundlach, R. H. Price, and J. Pullin, Phys. Rev. D **49**, 890 (1994).
[5] D. Garfinkle, Phys. Rev. D **51**, 5558 (1995).
[6] R. S. Hamadé and J. M. Stewart, Classical Quantum Gravity **13**, 497 (1996).
[7] A. Akbarian and M. W. Choptuik, Phys. Rev. D **92**, 084037 (2015).
[8] R.-G. Cai and Y. S. Myung, Phys. Rev. D **56**, 3466 (1997).
[9] M. Shibata, K. Nakao, and T. Nakamura, Phys. Rev. D **50**, 7304 (1994).
[10] T. Harada, T. Chiba, K.-i. Nakao, and T. Nakamura, Phys. Rev. D **55**, 2024 (1997).
[11] J. Novak, Phys. Rev. D **57**, 4789 (1998).
[12] M. Salgado, D. Sudarsky, and U. Nucamendi, Phys. Rev. D **58**, 124003 (1998).
[13] M. Ruiz, J. C. Degollado, M. Alcubierre, D. Núñez, and M. Salgado, Phys. Rev. D **86**, 104044 (2012).
[14] J. C. Degollado, M. Salgado, and M. Alcubierre, Phys. Lett. B **808**, 135666 (2020).
[15] B. Boisseau, G. Esposito-Farèse, D. Polarski, and A. A. Starobinsky, Phys. Rev. Lett. **85**, 2236 (2000).
[16] L. Amendola, Phys. Rev. Lett. **86**, 196 (2001).
[17] C. Schimd, J.-P. Uzan, and A. Riazuelo, Phys. Rev. D **71**, 083512 (2005).
[18] M. Salgado, Classical Quantum Gravity **23**, 4719 (2006).

[19] T. Damour and G. Esposito-Farese, Classical Quantum Gravity **9**, 2093 (1992).
[20] M. Alcubierre, *Introduction to 3+1 Numerical Relativity*, International Series of Monographs on Physics (Oxford University Press, Oxford, 2008).
[21] M. Salgado, D. M.-d. Río, M. Alcubierre, and D. Núñez, Phys. Rev. D **77**, 104010 (2008).
[22] C. Bona, J. Massó, E. Seidel, and J. Stela, Phys. Rev. Lett. **75**, 600 (1995).
[23] M. Alcubierre, Phys. Rev. D **55**, 5981 (1997).
[24] M. Alcubierre, Classical Quantum Gravity **20**, 607 (2003).
[25] T. W. Baumgarte and S. L. Shapiro, Phys. Rev. D **59**, 024007 (1998).
[26] M. Shibata and T. Nakamura, Phys. Rev. D **52**, 5428 (1995).
[27] M. Alcubierre and M. D. Mendez, Gen. Relativ. Gravit. **43**, 2769 (2011).
[28] J. D. Brown, Phys. Rev. D **79**, 104029 (2009).
[29] M. Campanelli, C. O. Lousto, P. Marronetti, and Y. Zlochower, Phys. Rev. Lett. **96**, 111101 (2006).
[30] M. Alcubierre and J. M. Torres, Classical Quantum Gravity **32**, 035006 (2015).
[31] M. Alcubierre, J. C. Degollado, D. Núñez, M. Ruiz, and M. Salgado, Phys. Rev. D **81**, 124018 (2010).
[32] S. Hod and T. Piran, Phys. Rev. D **55**, R440 (1997).
[33] T. W. Baumgarte, Phys. Rev. D **98**, 084012 (2018).
[34] C. Gundlach, Phys. Rev. D **55**, 695 (1997).
[35] D. Hilditch, T. W. Baumgarte, A. Weyhausen, T. Dietrich, B. Brügmann, P. J. Montero, and E. Müller, Phys. Rev. D **88**, 103009 (2013).
[36] D. R. Brill and R. W. Lindquist, Phys. Rev. **131**, 471 (1963).
[37] K. Eppley, Phys. Rev. D **16**, 1609 (1977).